Available online at: www. Ijcoe.org

# Integrated Probabilistic Tsunami Hazard and Spectral Energy Analysis of the Makran Subduction Zone: Deriving Hydrodynamic Design Envelopes for Critical Marine Infrastructure near the Strait of Hormuz

**Mahmood Reza Akbarpour Jannat[1*]; Mohammad Hossein Kazeminezhad[2]**

[1*] *Iranian National Institute for Oceanography and Atmospheric Science, No.3, Etemad Zadeh St., Fatemi Ave, P.C: 1411813389, Tehran, Iran, *(Corresponding author) E-mail: akbarpour@inio.ac.ir*
[2] *Iranian National Institute for Oceanography and Atmospheric Science, No.3, Etemad Zadeh St., Fatemi Ave, P.C: 1411813389, Tehran, Iran, E-mail: mkazeminezhad@inio.ac.ir*

## ARTICLE INFO

*Article History:*
Received: 05 Nov 2025
Accepted: 24 Feb 2026

*Keywords:*
**Makran Subduction Zone**
**Probabilistic Tsunami Hazard Assessment (PTHA)**
**Hydrodynamic Design Envelopes**
**Time-Frequency Analysis**
**Strait of Hormuz**

## ABSTRACT

The strategic development of energy infrastructure along the Makran Subduction Zone (MSZ), particularly the Kooh Mobarak Terminal near the Strait of Hormuz, demands a rigorous transition from deterministic assessments to risk-informed frameworks. While the eastern MSZ has a well-documented seismic history, the western segment presents a critical latent threat due to strong inter-seismic coupling. This study introduces an integrated framework combining Probabilistic Tsunami Hazard Assessment (PTHA) with advanced time-frequency analysis to quantify multi-dimensional risks. Building upon high-resolution hydrodynamic simulations, site-specific "Hydrodynamic Design Envelopes" were derived to explicitly correlate wave height and current velocity. Results indicate that for the 975-year Maximum Credible Earthquake, the nearshore breakwater faces extreme compound loads, with wave heights approaching 3.0 m and velocities exceeding 2.3 m/s, necessitating a shift to hydrodynamic drag-based design criteria. Furthermore, spectral characterization using Welch's method and Continuous Wavelet Transform (CWT) identifies dominant energy bands at 24–30 and ~64 minutes, providing vital geometric constraints to avoid destructive harbor resonance. Additionally, time-frequency analysis reveals a significant lag between initial arrival and peak energy flux, demonstrating that hazardous agitation persists for over 4 hours. These findings underscore the imperative of adopting a performance-based design philosophy that accounts for probabilistic exceedance, resonance avoidance, and extended operational exclusion windows.

## 1. Introduction

The strategic expansion of critical energy infrastructure along coastal margins, particularly in tectonically complex regions like the northwestern Indian Ocean, necessitates a paradigm shift in natural hazard assessment. We are moving from deterministic, single-scenario analyses toward comprehensive, risk-informed frameworks that account for the stochastic nature of extreme events. The Makran Subduction Zone (MSZ), stretching approximately 900 km along the coasts of Iran and Pakistan, represents a formidable tsunamigenic structure formed by the northward subduction of the Arabian Plate beneath the Eurasian Plate. Characterized by an exceptionally thick accretionary wedge and a shallow dip angle, the MSZ possesses the geomorphological capacity to generate mega-thrust earthquakes exceeding Mw 8.5. The catastrophic tsunami of November 28, 1945 ($M_w$ 8.1), which claimed over 4,000 lives and devastated the coasts of Pakistan, Iran, and Oman, serves as a stark historical benchmark (Heidarzadeh et al., 2008; Rajendran et al., 2008). However, the scarcity of instrumental records for earlier events, combined with the long recurrence intervals of mega-thrust ruptures, introduces significant epistemic uncertainty into hazard estimations. For the rapidly industrializing Iranian coastline, specifically the Oil Terminal situated near the strategic chokepoint of the Strait of Hormuz, the potential for a large-scale tsunami poses a dual threat: an immediate risk to coastal assets and a broader strategic risk to global energy security. Consequently, ensuring the resilience of complex marine facilities such as breakwaters, jetties, and Moorings requires a rigorous quantification of hazard that transcends historical retrospection.

Traditionally, tsunami hazard assessments in the Makran region have predominantly relied on Deterministic Tsunami Hazard Assessment (DTHA). These approaches simulate specific "worst-case" scenarios based on maximum credible earthquakes to define ultimate limit states for inundation mapping. In a recent companion study, Kazeminezhad et al. (2026) provided a high-resolution deterministic assessment for the Kooh Mobarak region. That investigation was pivotal in identifying the critical threat posed by the western Makran segment, a region previously considered a "seismic gap", and highlighted the compound risks of tidal interactions. While deterministic scenarios are essential for emergency response planning and understanding the physical upper bounds of flooding, they inherently lack the temporal dimension of risk. They do not quantify the probability of exceedance over the operational lifespan of a structure, typically 50 to 100 years for critical infrastructure. Engineering stakeholders require probabilistic metrics to optimize capital investment against risk, balancing safety with economic viability. This necessitates a Probabilistic Tsunami Hazard Assessment (PTHA) that integrates seismic recurrence rates with hydrodynamic modeling to derive hazard curves, thereby addressing the aleatory variability in source characteristics.

Over the past decade, the scientific community has made significant strides in quantifying the probabilistic tsunami hazard in the Makran region. Heidarzadeh and Kijko (2011) conducted one of the pioneer PTHA studies for the entire MSZ using Monte Carlo simulations, estimating the probability of wave heights exceeding 5 meters. Subsequently, El-Hussain et al. (2016) applied a logic-tree approach to account for epistemic uncertainties in source parameters for the Omani coast. As computational power increased, recent studies have moved towards stochastic source modeling to capture rupture complexities. Rashidi et al. (2020) and Salah et al. (2021) incorporated heterogeneous slip distributions to refine hazard estimates for the eastern and central Makran. More specifically targeting the Iranian coast, Zafarani et al. (2022) performed a PTHA for the western Makran, providing valuable return period estimates for coastal cities. Most recently, Momeni and Goda (2024) presented a comprehensive PTHA using logic trees and stochastic rupture sources, investigating uncertainties associated with segmentation, geometry, and slip heterogeneity. Their work represents the current state-of-the-art, highlighting that tsunami heights are highly sensitive to the location of large slip areas and nearshore bathymetry.

Despite these advancements, a critical gap persists in the existing literature, including the most recent probabilistic studies. The vast majority of PTHA efforts in the region focus almost exclusively on maximum wave amplitude (run-up) as the primary intensity measure. While wave height is the governing parameter for flood mapping and crest elevation design, it fails to capture the spectral characteristics, time-frequency evolution, and kinetic energy of the tsunami wave train. Tsunami waves are not solitary pulses; they are broadband signals containing energy across a wide range of frequencies. When these long-period waves interact with the shallow continental shelf and semi-enclosed water bodies like harbor basins, the phenomenon of resonance can occur. If the dominant period of the incoming wave train aligns with the fundamental natural frequency of the harbor (Helmholtz mode), amplification factors can far exceed those predicted by simple run-up models (Rabinovich, 2009). This resonant response can induce severe harbor agitation and dangerous currents, disrupting port operations and causing damage to moored vessels even when the incident wave height appears manageable. Furthermore, for offshore structures like Moorings, the hydrodynamic drag force, which scales with the square of current velocity ($V^2$), is often the failure mechanism, yet probabilistic assessments of current velocity remain rare.

The application of advanced signal processing techniques to tsunami hazard assessment in the Makran region remains largely unexplored. Techniques such as the Fast Fourier Transform (Welch's Method) for identifying dominant energy bands and the Continuous Wavelet Transform (CWT) for analyzing the temporal localization of this energy are standard in other fields but absent in Makran tsunami studies. Understanding not just *how high* the wave is, but *when* the peak energy arrives, *what frequencies* it carries, and *how long* it persists in resonance-prone bands, is vital for defining operational downtime windows and resilience strategies.

This study aims to bridge the gap between traditional probabilistic assessments and advanced hydrodynamic characterization, providing a holistic framework for coastal resilience at the Kooh Mobarak terminal. Building upon the validated numerical models of the companion study (Kazeminezhad et al., 2026), this research shifts the focus from "what is possible" to "what is probable" and "how the energy evolves." The specific contributions of this paper are threefold. Firstly, we develop high-resolution hazard curves and novel hydrodynamic design envelopes for the Kooh Mobarak terminal, explicitly correlating wave height and current velocity for return periods relevant to engineering design (475 and 975 years). This facilitates a "Performance-Based Design" approach where different limit states (serviceability vs. ultimate) are checked against different hazard levels. Secondly, we employ spectral analysis using Welch's method to identify the dominant periods of the expected tsunami waves and calculate the critical resonant lengths for future port basins, providing a proactive geometric constraint for harbor designers. Finally, utilizing Wavelet analysis, we visualize the time-frequency evolution of the tsunami energy, quantifying the duration of hazardous conditions. This integration of PTHA with spectral analysis provides a robust scientific basis for the safe development of strategic infrastructure in the Strait of Hormuz region.

## 2. Study Area and Tectonic Context

The geographical focal point of this research is the coastal zone of Kooh Mobarak and the adjacent Oil Terminal (OT), situated strategically at the entrance to the Strait of Hormuz in southeastern Iran (approximate coordinates: 25.85°N, 57.27°E). As illustrated in Figure 1, this region represents a pivotal node in the global energy transit network. The development of the OT serves as a critical strategic asset, facilitating the export of crude oil directly into the Gulf of Oman and effectively bypassing the potential chokepoint of the Strait of Hormuz. Given the high-value infrastructure involved, including storage tanks, moorings (Ms), and extensive breakwater systems, and the dense concentration of maritime traffic, the resilience of this zone against extreme hydrodynamic loads is of paramount national and international importance. The coastal geomorphology of Kooh Mobarak is characterized by a relatively wide continental shelf and a complex network of tidal creeks (Khors), features that can significantly modulate tsunami wave amplification and inundation patterns. To accurately capture these local bathymetric influences, the study area is enclosed within a high-resolution computational grid, which allows for detailed hydrodynamic modeling of nearshore interactions.

Tectonically, the study area lies directly north of the Western Makran Subduction Zone (W-MSZ), an active convergent boundary where the dense oceanic lithosphere of the Arabian Plate subducts beneath the continental Eurasian Plate. Geodetic measurements indicate a convergence rate increasing from approximately 19.5 mm/yr in the eastern Makran to roughly 27 mm/yr in the western segment (Vernant *et al*., 2004). This subduction process has resulted in the formation of an exceptionally thick accretionary sediment wedge (exceeding 7 km), a geological feature associated with the generation of tsunamis characterized by long periods and significant run-up potentials. The MSZ is structurally segmented into three distinct rupture zones: Western, Central, and Eastern Makran (Figure 1). While the eastern segment (offshore Pakistan) has a well-documented history of major tsunamigenic earthquakes, most notably the catastrophic 1945 $M_w$ 8.1 event, the western segment adjacent to Jask has experienced a prolonged period of seismic quiescence spanning several centuries. This lack of historical seismicity has led to its classification as a "seismic gap" (Byrne *et al*., 1992).

However, the absence of recent large earthquakes in the Western Makran should not be misinterpreted as a lack of hazard. Recent inversions of GPS velocity fields and elastic block modeling suggest a high degree of inter-seismic coupling (locking) along the plate interface in this region (Frohling and Szeliga, 2016). This indicates that the fault is accumulating significant elastic strain, rather than releasing stress through aseismic creep, thereby possessing the potential to generate megathrust earthquakes exceeding $M_w$ 8.5. To operationalize this tectonic framework for Probabilistic Tsunami Hazard Assessment (PTHA), the fault interface is conceptualized as a geometric grid of rectangular unit sources (sub-faults), superimposed on the physical map in Figure 1. This discretization comprises two parallel rows aligned with the trench strike: the shallow 'a-series' representing the up-dip interface closer to the deformation front, and the deeper 'b-series' corresponding to the down-dip interface. This configuration allows for the simulation of heterogeneous slip distributions and the definition of location-specific rupture scenarios, ranging from localized western events to full-margin ruptures, that form the basis of the probabilistic source model employed in this study.

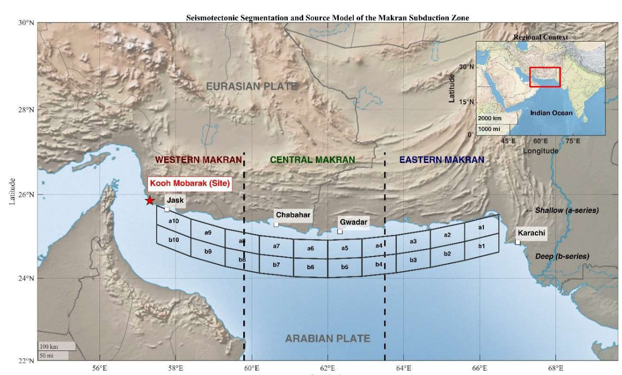


**Figure 1. Seismotectonic setting and source characterization model of the Makran Subduction Zone (MSZ). The map illustrates the tripartite segmentation of the margin into Western, Central, and Eastern Makran sectors, separated by vertical dashed boundaries. The superimposed rectangular grid depicts the spatial discretization of the fault interface used for the probabilistic tsunami hazard assessment (PTHA), comprising a shallow 'a-series' (updip interface) and a deeper 'b-series' (downdip interface). The red star indicates the strategic location of the Kooh Mobarak project site, situated directly north of the Western Makran seismic gap. (Inset) Regional context of the study area within the northwestern Indian Ocean basin.**

## 3. Methodology

### 3.1 Numerical Modeling Framework

To derive the extensive hydrodynamic dataset required for the Probabilistic Tsunami Hazard Assessment

**Table 1. Seismogenic source parameters and statistical recurrence rates for the deterministic fault rupture scenarios used in the PTHA framework.**

| Magnitude (Mw) | Mean Annual Rate(λ) [1/yr]* | Slip (u) [m] | Rupture Dimensions ($L$×$W$) [km] | Seismic Moment ($M_0$) [N·m] | Scenario ID** |
|---|---|---|---|---|---|
| **8.0** | 0.0080 | 4.0 | 200 × 50 | $1.26×10^{21}$ | M8.0-W<br>M8.0-C<br>M8.0-E |
| **8.4** | 0.0038 | 10.0 | 300 × 50 | $4.47×10^{21}$ | M8.4-W<br>M8.4-C<br>M8.4-E |
| **8.7** | 0.0021 | 17.0 | 500 × 50 | $1.26×10^{22}$ | M8.7-W<br>M8.7-C<br>M8.7-E |
| **8.9** | 0.0013 | 23.0 | 700 × 50 | $2.51×10^{22}$ | M8.9-W<br>M8.9-E |
| **9.0** | 0.0011 | 27.0 | 900 × 50 | 3.55×1022 | M9.0-C |

*Mean annual rates (λ) are derived from the return periods ($T$) provided by El-Hussain et al. (2016), calculated as λ = 1/$T$
** The suffixes W, C, and E in the Scenario ID denote the Western, Central, and Eastern segments of the Makran Subduction Zone, respectively. Seismic moment ($M_0$) is calculated assuming a shear modulus (μ) of 30 GPa.

(PTHA) and the subsequent spectral analysis, a systematic numerical modeling campaign was executed. The generation, propagation, and coastal inundation phases of the tsunami were simulated using the ComMIT/MOST (Method of Splitting Tsunami) system. Developed by NOAA's Pacific Marine Environmental Laboratory, this model serves as a standard operational tool for tsunami forecasting due to its validated capability to handle trans-oceanic propagation and complex nearshore interactions. The modeling framework employed in this study is underpinned by the Nonlinear Shallow Water Equations (NSWE), formulated in spherical coordinates to explicitly account for the Earth's curvature, which becomes increasingly significant over the large spatial scales of the Makran Subduction Zone. The hydrodynamic solver is governed by the fundamental principles of conservation of mass and momentum, incorporating terms to represent the Coriolis force and bottom friction. The frictional dissipation is parameterized using the Manning's roughness coefficient, which was set to a standard value of 0.025 $m^{-1/3}s$ for the nearshore domain to represent the seabed roughness characteristics of the region. Rather than solving the fully coupled system simultaneously, the model utilizes a dimensional splitting numerical scheme. This algorithm decomposes the governing equations into two orthogonal one-dimensional problems, which are solved sequentially. This approach significantly optimizes computational efficiency without compromising numerical stability, allowing for the simulation of long-duration wave trains necessary for spectral analysis. For a detailed mathematical derivation of the governing equations and the specific numerical discretization techniques employed, the reader is referred to the foundational work of Titov and Synolakis (1998) and the comprehensive methodology presented in our companion study, Kazeminezhad et al. (2026).

The reliability of nearshore hydrodynamic estimates is intrinsically linked to the resolution of the spatial discretization and the quality of the bathymetric data. To bridge the scale gap between the basin-wide propagation in the Indian Ocean and the localized wave transformation at the Kooh Mobarak coastline, a dynamic nested grid strategy was implemented. As illustrated in Figure 2, the computational domain is structured into three telescoping grids that progressively refine the spatial resolution. The outermost regional grid (Grid A) encompasses the entire Northern Indian Ocean with a resolution of 2 arc-minutes, sufficient to capture the source generation and initial directivity of the tsunami energy. Nested within this is the intermediate grid (Grid B), which focuses on the Gulf of Oman and the entrance to the Strait of Hormuz with a resolution of 30 arc-seconds, resolving the shelf slope processes. Finally, the innermost local grid (Grid C) targets the specific study area of Kooh Mobarak and the Jask terminal with a high-resolution mesh of 3 arc-seconds (approximately 90 meters). This fine-scale resolution is critical for accurately resolving the non-linear shoaling effects, flow constriction around breakwaters, and the run-up onto the complex coastal topography. The bathymetric and topographic data driving these grids were constructed by seamlessly integrating the GEBCO global dataset for deep waters with high-resolution SRTM digital elevation models and local hydrographic surveys for the nearshore zone, ensuring a continuous and artifact-free representation of the seafloor.

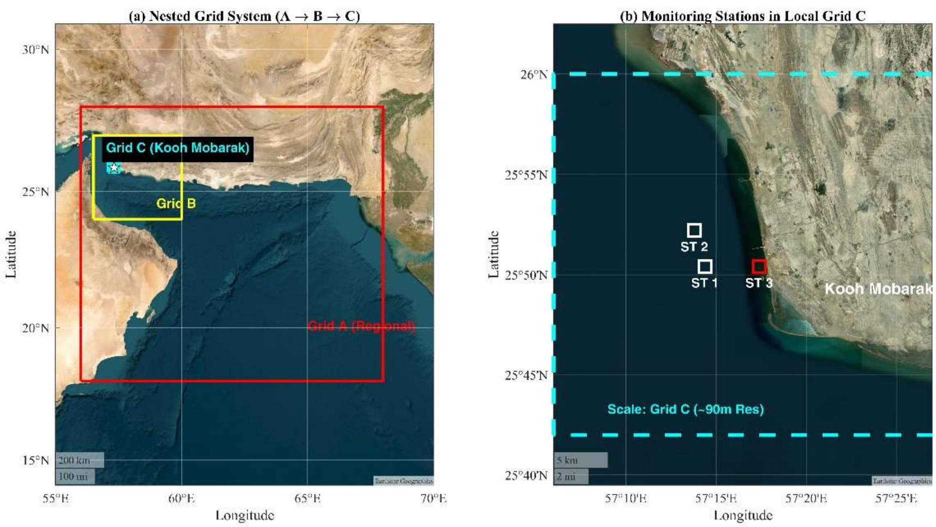


**Figure 2. Configuration of the computational domains and monitoring stations employed for the hydrodynamic simulations. (a) The nested grid system hierarchy consisting of three dynamically coupled layers: the regional Grid A (covering the Northern Indian Ocean), the intermediate Grid B (focusing on the Gulf of Oman), and the high-resolution local Grid C (targeting the Kooh Mobarak coastal zone). (b) Detailed view of the local Grid C domain, illustrating the spatial distribution of virtual gauge points relative to the coastline. Stations ST 1 and ST 2 are positioned in the offshore zone (~50 m depth) to capture deep-water wave characteristics, while ST 3 is located in the nearshore zone (~10 m depth) adjacent to the nearshore to assess shoaling amplification and impact loads.**

Within this high-resolution local domain, specific virtual monitoring stations were established to extract the time-series data necessary for the subsequent spectral and probabilistic analyses. As depicted in Figure 2b, three strategic locations were selected to capture the hydrodynamic regime transition. Stations ST 1 and ST 2 are situated in the offshore zone at water depths of approximately 45 to 50 meters, representative of the operational environment for Single Point Moorings (SPMs) and deep-draft tanker navigation. Conversely, station ST 3 is located in the nearshore zone at a depth of roughly 10 meters, immediately adjacent to the nearshore of Kooh Mobarak. This spatial configuration allows for a distinct comparative analysis of how the tsunami hazard amplifies as the waves transition from the linear deep water regime to the non-linear shallow water regime. The time histories of water surface elevation and depth averaged current velocity recorded at these stations form the raw input for the spectral energy density calculations and the construction of the hazard curves.

The probabilistic framework of this study is founded upon a suite of twelve deterministic fault rupture scenarios, defined to encapsulate the epistemic and aleatory uncertainties inherent in the seismic source characterization. As summarized in Table 1, these scenarios span a comprehensive range of moment magnitudes from $M_w$ 8.0 to 9.0, spatially distributed across the Western, Central, and Eastern tectonic segments of the Makran trench (shown in Figure 1). To ensure physical consistency, the geometric fault parameters for each scenario, including rupture length, width, and average slip, were derived from the empirical scaling laws of Wells and Coppersmith (1994). The maximum hydrodynamic values (peak wave height and peak current velocity) extracted from these twelve deterministic simulations serve as the primary dataset. By weighting these deterministic outputs with their respective mean annual recurrence rates, we construct the probabilistic hazard curves and design envelopes that constitute the core findings of this research.

### 3.2. Seismotectonic Setting and Probabilistic Framework

The foundation of any robust Probabilistic Tsunami Hazard Assessment (PTHA) lies in the accurate characterization of the seismogenic source and the mathematical framework used to quantify the temporal likelihood of extreme events. The Makran Subduction Zone (MSZ) constitutes the active convergent boundary where the dense oceanic lithosphere of the

Arabian Plate subducts beneath the continental Eurasian Plate. This large-scale tectonic process, occurring at a convergence rate increasing from approximately 19.5 mm/yr in the east to roughly 27 mm/yr in the west (Vernant et al., 2004), serves as the primary engine for elastic strain accumulation. Geological evidence suggests that the MSZ is characterized by an exceptionally thick sedimentary wedge (>7 km) and a shallow dip angle. Such a geometric configuration is particularly conducive to generating tsunamigenic earthquakes because it allows rupture propagation into the shallow up-dip portion of the megathrust, potentially leading to large vertical seafloor displacements and significant water column perturbation (Smith et al., 2013). However, the translation of this continuous tectonic loading into discrete seismic release is highly heterogeneous along the strike of the subduction zone. While the eastern segment (offshore Pakistan) has a documented history of large earthquakes, most notably the 1945 $M_w$ 8.1 event, the western segment (offshore Iran), situated directly adjacent to the strategic Strait of Hormuz, has exhibited a puzzling seismic quiescence for several centuries. This "seismic gap" presents a critical challenge for hazard assessment: does the absence of historical seismicity imply aseismic creep, or does it indicate a locked fault late in its seismic cycle? Recent elastic block modeling and GPS velocity fields strongly support the latter, estimating a high degree of interseismic coupling in the western Makran (Frohling and Szeliga, 2016). Therefore, relying solely on historical catalogs would catastrophically underestimate the hazard for the Jask region. Instead, a seismotectonic approach based on the conservation of seismic moment budget is required to estimate recurrence rates.

### 3.2.1 Seismic Recurrence Rates and Source Characterization

Quantifying the mean recurrence interval ($T_r$) for potential megathrust ruptures in the MSZ requires synthesizing geodetic data, paleoseismic evidence, and empirical scaling laws. In this study, we adopt the recurrence parameters derived by El-Hussain et al. (2016), who utilized a logic-tree approach to account for epistemic uncertainties in the maximum magnitude ($M_{max}$) and the b-value of the Gutenberg-Richter relationship. Their model balances the seismic moment accumulation (derived from the ~19 mm/yr convergence rate) with the moment release of characteristic earthquakes, providing a physically consistent basis for PTHA in data-poor regions.

The recurrence model integrated into this study is detailed in Table 1. The framework conceptualizes the MSZ as three segmented rupture zones: Western, Central, and Eastern. This segmentation allows for the spatial differentiation of hazard, ensuring that the specific threat to the Jask terminal from the near-field western segment is explicitly captured. For each tectonic segment, characteristic earthquakes with moment magnitudes ($M_w$) of 8.0, 8.4, 8.7, and 8.9 are defined to represent a spectrum of energy release scenarios. Furthermore, a "worst-case" full-margin rupture scenario ($M_w$ 9.0) is included in the Central segment to account for the possibility of multi-segment cascading rupture, a phenomenon observed in other subduction zones (e.g., the 2004 Sumatra and 2011 Tohoku events). The estimated mean return periods range from approximately 125 years for moderate tsunamigenic events (Mw 8.0) to 946 years for catastrophic $M_w$ 9.0 events. These values imply that while smaller events are relatively frequent, the accumulation of strain required for a full-scale rupture takes nearly a millennium, consistent with the long seismic gaps observed in the historical record.

### 3.2.2 The Poissonian Probability Model

The core of the PTHA methodology involves converting the mean recurrence intervals of seismic sources into a probability of exceeding specific hydrodynamic intensity measures (e.g., wave height or current velocity) at the site of interest over a given timeframe. Following standard practice in engineering hazard analysis, the temporal occurrence of tsunamigenic earthquakes is modeled as a Poisson process. The Poisson model assumes that earthquake occurrences are stochastic, memoryless events; meaning the probability of an earthquake occurring in the next interval is independent of when the last earthquake occurred (Heidarzadeh and Kijko, 2011). While time-dependent models (e.g., Brownian Passage Time) might be more physically rigorous for faults with well-known earthquake histories, the large uncertainties surrounding the last rupture date of the western Makran make the time-independent Poisson model the most prudent and robust choice for design purposes.

Under the Poisson assumption, the probability $P(t)$ that at least one earthquake of a specific magnitude class $m$ will occur during a specified exposure time $t$ is expressed as:

$$P(E>0 \mid t, \lambda_m)=1-e^{-\lambda m t} \quad (1)$$

Where $\lambda_m=1/T_r$ represents the mean annual rate of occurrence for the magnitude class $m$. However, the hazard at a specific coastal site like Jask is not determined by a single scenario but is the aggregate of risks from all possible sources. Therefore, we calculate the **total mean annual rate of exceedance**, $\Lambda(h)$, for a specific hydrodynamic threshold $h$ (e.g., wave height > 2.0 m). This is achieved by summing the contributions from all $N$ potential rupture scenarios (Western, Central, and Eastern) that are capable of generating waves exceeding $h$ at the site:

$$\Lambda(h) = \sum_{i=1}^{N} v_i \cdot P(H > h \mid Senario_i) \quad (2)$$

In this equation, $v_i$ is the annual rate of occurrence for Scenario $i$ (derived from Table 1), and $P(H > h|Scenario_i)$ acts as a binary indicator function (Heaviside step function): it equals 1 if the deterministic simulation of Scenario $i$ produces a wave height greater than $h$ at the Jask terminal, and 0 otherwise. The hydrodynamic inputs for this aggregation are derived directly from the high-resolution numerical simulations presented in our companion study (Kazeminezhad et al., 2026). In that study, the nonlinear shallow water equations were solved using the validated ComMIT/MOST model over a nested grid system, achieving a resolution of 90 meters in the nearshore zone. By coupling these deterministic hydrodynamic results with the probabilistic recurrence rates, we construct site-specific hazard curves.

This study evaluates the hazard for two distinct exposure times: $t=50$ years and $t=100$ years. The 50-year horizon aligns with the typical design life of standard maritime structures and is used to define "Operating Basis Earthquake" (OBE) conditions. The 100-year horizon is selected to address the extended lifespan and higher safety factors required for critical energy infrastructure like oil terminals, corresponding to "Maximum Design Earthquake" (MDE) considerations. This dual-timeframe approach provides stakeholders with a comprehensive risk profile, facilitating decisions that balance immediate operational continuity with long-term asset survivability.

## 4. Results and Discussion

### 4.1 Probabilistic Tsunami Hazard Assessment (PTHA)

Building upon the probabilistic framework established in the preceding section, this portion of the study quantifies the site-specific tsunami hazard for the Kooh Mobarak region and its associated marine facilities. By aggregating the contributions of the twelve deterministic rupture scenarios, weighted by their respective recurrence rates derived from the seismotectonic analysis, we derive a comprehensive risk profile. The results are presented through two complementary analytical lenses: Probability of Exceedance Curves for individual hydrodynamic parameters, and Integrated Hydrodynamic Design Envelopes that correlate wave height and current velocity with standard engineering return periods.

#### 4.1.1 Hazard Curves for Elevation and Velocity

The hazard curves for maximum wave height ($H_{max}$) and current velocity ($V_{max}$), illustrated in Figures 3 and 4, reveal a characteristic "stepped" morphology rather than a smooth exponential decay. This stepwise behavior is a direct consequence of the logic-tree approach and the discrete nature of the characteristic earthquake scenarios used in the PTHA, which range from $M_w$ 8.0 to 9.0. Each inflection point on the curve corresponds to the activation of a more severe, albeit less frequent, fault rupture segment, such as the transition from frequent Western Makran events to rare full-margin ruptures. A spatial comparison between the stations reveals a profound bathymetric amplification effect. In the deeper waters characteristic of the offshore zones (ST 1 and ST 2, depths ~45–50 m), the hazard curves decay rapidly. For a 10% probability of exceedance in 50 years, approximating a 475-year return period, the expected wave heights remain moderate, ranging between 0.8 m and 0.9 m, with current velocities staying below 0.5 m/s. This indicates that in the deep-water regime, the tsunami energy remains primarily potential rather than kinetic.

In stark contrast, the nearshore regime represented by the nearshore zone (ST 3, depth ~10 m) exhibits a dramatic intensification of hazard due to shoaling processes. The wave height hazard curve shifts significantly, indicating much higher values for equivalent probability levels. More critically, the velocity hazard curve shows that velocities exceeding 1.5 m/s have a tangible probability of occurrence. This non-linear amplification underscores that determining hazard levels solely based on offshore observation points would drastically underestimate the hydrodynamic loads acting on coastal defense structures.

#### 4.1.2 Hydrodynamic Design Envelopes

To translate these probabilistic findings into actionable engineering criteria, the data were synthesized into "Hydrodynamic Design Envelopes" shown in Figure 5. These dual-axis charts plot both the Design Wave Height and Design Current Velocity as a continuous function of the Return Period ($T_r$), allowing for a Performance-Based Design (PBD) evaluation at two standard levels: the Operating Basis Earthquake (OBE, 475 years) for serviceability, and the Maximum Credible Earthquake (MCE, 975 years) for ultimate survival. Detailed analysis of the design envelopes identifies the Breakwater Head as the most critical asset subject to severe loading. At the 475-year return period, the design wave height is calculated at 1.90 m, accompanied by a design current velocity of 1.30 m/s. These values suggest that even for the serviceability limit state, the breakwater armor units must be sized to withstand significant dynamic pressure. As the return period extends to the MCE level of 975 years, the design values escalate to approximately 2.85 m for wave height and over 2.0 m/s for current velocity. Notably, the current velocity curve at ST 3 exhibits a steep gradient between the 100-year and 400-year return periods, implying that once the hazard threshold corresponding to Western Makran ruptures is crossed, the flow regime transitions rapidly from a low-velocity oscillation to a high-velocity hydraulic bore. This necessitates that toe protection designs account for high-shear scouring flows that can destabilize the structure's foundation.

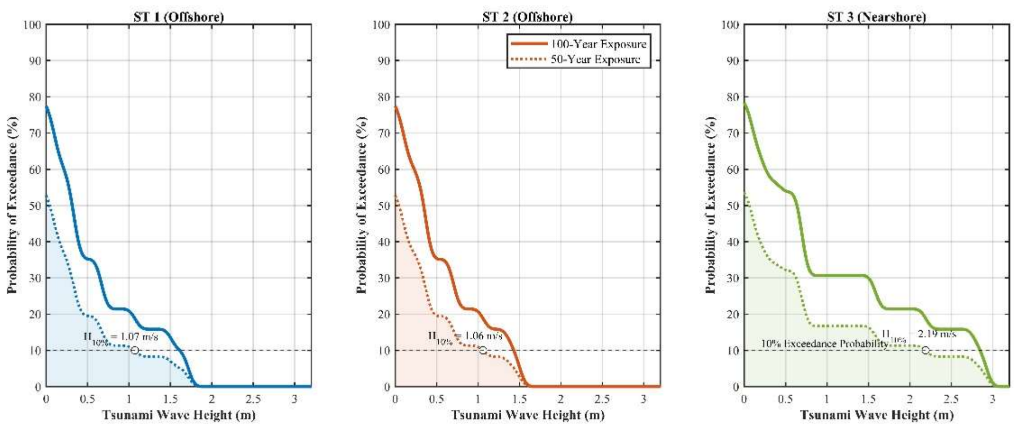


**Figure 3. Probabilistic tsunami hazard curves for maximum wave height ($H_{max}$) at three strategic monitoring stations: ST 1 and ST 2 (Offshore) and ST 3 (Nearshore). The solid and dotted lines represent the probability of exceedance over exposure periods of 100 years and 50 years, respectively. The horizontal dashed line marks the 10% probability of exceedance threshold, with annotated values highlighting the expected wave heights for the 50-year exposure time. Note the significant amplification of hazard at the nearshore station (ST 3) compared to the offshore locations due to shoaling effects.**

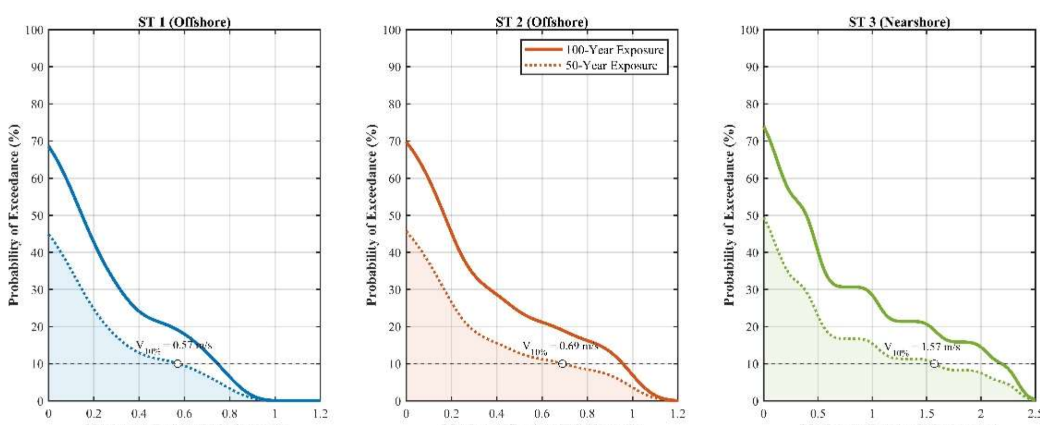


**Figure 4. Probabilistic hazard curves for maximum tsunami-induced current velocity ($V_{max}$) at the designated monitoring stations. Similar to the wave height trends, the nearshore station (ST 3) exhibits a markedly higher probability of experiencing extreme velocities compared to the offshore sites (ST 1 and ST 2). The annotated values corresponding to a 10% probability of exceedance in 50 years (e.g., 1.57 m/s at ST 3 versus ~0.6 m/s offshore) serve as critical inputs for assessing hydrodynamic drag forces and scour potential.**

Conversely, the design envelopes for the offshore stations (ST 1 and ST 2) exhibit a fundamentally different hydrodynamic behavior. At ST 1, for the 475-year return period, the design wave height is 0.79 m with a current velocity of 0.43 m/s, while at ST 2, these values are slightly higher at 0.83 m and 0.56 m/s, respectively. Although these wave heights are manageable, the current velocities in the "Low Hazard Zone" are negligible. However, as the return period approaches the MCE event, velocities rise towards 0.8–0.9 m/s. While significantly lower than the nearshore values, these currents acting on the immense hull area of Very Large Crude Carriers (VLCCs) can generate massive hydrodynamic drag forces ($F_D \propto V^2$). Therefore, while the breakwater design is governed by scouring and impact loads, the offshore facility design must prioritize the fatigue limit and peak-load capacity of mooring hawsers and subsea pipeline connections to prevent rupture during rare mega-thrust events.

## 4.2 Spectral and Time-Frequency Dynamics

While probabilistic hazard curves provide essential metrics for establishing design return periods, they inherently compress the temporal complexity of tsunami waves into single peak values. However, tsunami interaction with coastal infrastructure is a

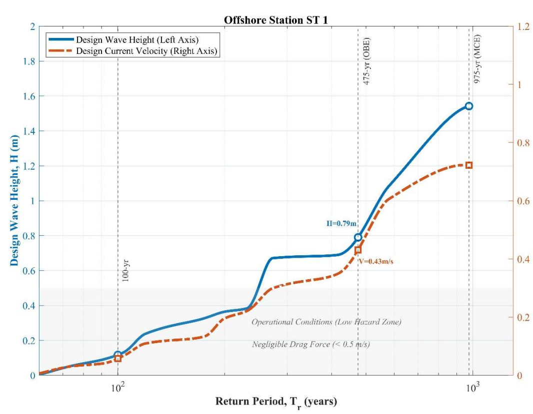


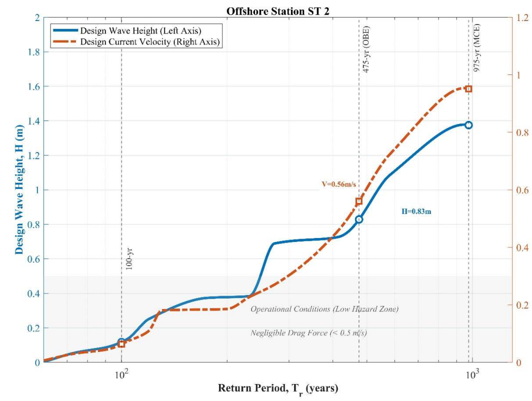


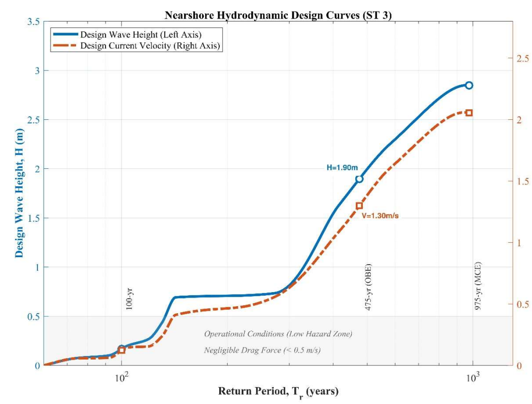


**Figure 5. Integrated hydrodynamic design envelopes derived from PTHA for the offshore locations (ST 1 and ST 2), and the nearshore station (ST 3). The dual-axis plots correlate Design Wave Height (solid blue line, left axis) and Design Current Velocity (dashed orange line, right axis) as a function of the Return Period ($T_r$). Specific design values are annotated for the Operating Basis Earthquake (OBE, 475 years) and Maximum Credible Earthquake (MCE, 975 years). Note the drastic non-linear amplification of current velocity at the nearshore station (ST 3) reaching >2.0 m/s for the MCE, contrasting with the deeper offshore stations where velocities remain largely below 1.0 m/s but are sufficient to induce drag loads on moored vessels. The shaded grey regions indicate the low-hazard operational zone with negligible drag forces.**

dynamic process governed not only by amplitude but critically by the frequency content and duration of the wave train. Therefore, this section complements the PTHA by providing a rigorous spectral analysis of the simulated waveforms at the offshore control points (SPM 1), elucidating the energy distribution that drives harbor resonance and operational downtime.

### 4.2.1 Time-Domain Characteristics and Waveform Complexity

The temporal evolution of the free-surface elevation for the three governing tectonic scenarios, Central Makran

($M_w$ 9.0), Western Makran ($M_w$ 8.9), and Western Makran ($M_w$8.7), is visualized in Figure 6. A comparative analysis of these waveforms reveals that the tsunami signature is not a solitary soliton but a complex, dispersive wave train characterized by multiple crests and troughs. A critical hydrodynamic feature observed across all scenarios is the initial phase of the arrival. The waveforms exhibit a distinct leading depression (drawdown) prior to the arrival of the primary crest. For the offshore location, this drawdown reaches approximately -1.4 m for the M9.0-C scenario. This phenomenon is hydrodynamically significant for offshore loading terminals, as unexpected drops in water level can reduce the under keel clearance of deep draft tankers, posing a risk of grounding even before the destructive crest arrives. Furthermore, the time-domain comparison reinforces the findings of the deterministic assessment regarding the "Western Threat." The wave train generated by the Western $M_w$ 8.9 scenario exhibits an amplitude structure and period modulation remarkably similar to the catastrophic Central $M_w$ 9.0 event, with maximum elevations reaching 1.52 m compared to 1.71 m, respectively. This similarity confirms that the proximity of the western rupture zone compensates for the lower seismic moment, generating near-field energy fluxes comparable to far-field mega-thrusts.

### 4.2.2 Spectral Energy Distribution and Dominant Periods

To identify the frequency bands responsible for potential harbor resonance, the time-series data were transformed into the frequency domain using Welch's Periodogram method. The resulting Energy Spectral Density (ESD) is presented in Figure 7, where the power spectral density is plotted against wave period on a base-2 logarithmic scale to resolve low-frequency components. The spectral analysis uncovers a bi-modal energy distribution characteristic of the Makran basin response. The spectra for all three scenarios are dominated by two distinct energy peaks. The primary peak ($T_{p1}$) is consistently located at a period of approximately 64.0 minutes, representing the fundamental mode of the continental shelf oscillation

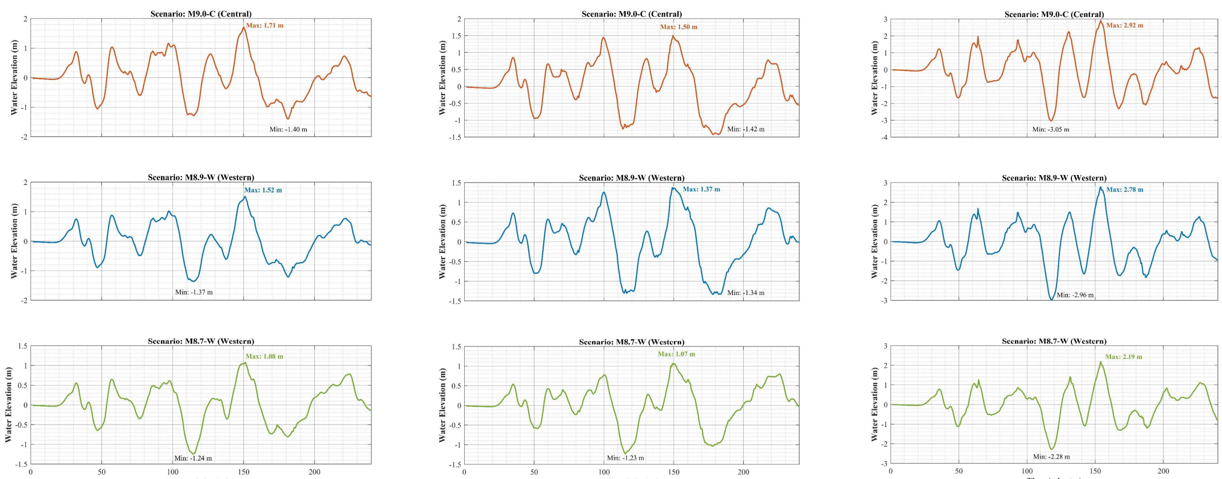


**Figure 6. Comparison of simulated tsunami waveforms at the offshore sites (ST 1 and ST 2) and nearshore station (ST 3) for the three governing rupture scenarios from left to right respectively.**

or the source duration effect. A secondary, yet highly energetic peak ($T_{p2}$) is observed in the 24.0 to 30.0-minute band.

The identification of these dominant periods provides a crucial geometric constraint for the design of the future Kooh Mobarak port basin. Semi-enclosed harbors act as high resonators; if the natural eigen-period of the basin aligns with these incoming energy bands, destructive resonance will occur. Specifically, the high energy concentration in the 24–30 minute band is particularly hazardous for medium-sized commercial ports, as it often corresponds to the fundamental Helmholtz mode of basins with typical dimensions (e.g., lengths of 2–3 km). Therefore, port layouts must be dimensioned such that their natural periods are detuned from these critical spectral peaks to prevent amplification of harbor agitation and currents. Comparing the scenarios, the M9.0-C event naturally contains the highest total energy (integral of the curve), yet the M8.9-W scenario follows closely, maintaining high energy density across the same critical frequency bands, further validating the necessity of considering western ruptures in resonance calculations.

### 4.2.3 Time-Frequency Evolution of Wave Energy

While the Fourier analysis identifies *which* frequencies carry the most energy, it does not reveal *when* these frequencies arrive or how they evolve over time. To visualize the non-stationary nature of the tsunami, a Continuous Wavelet Transform (CWT) was applied using the Morlet wavelet. Figure 8 presents the resulting wavelet power spectra (scalograms) for the three scenarios. The vertical axis represents the wave period (logarithmic scale), the horizontal axis represents time, and the color intensity signifies the energy density.

The scalograms reveal a distinct frequency dispersion pattern characteristic of distant tsunami propagation. The energy does not arrive as a monochromatic packet; instead, we observe a temporal separation of frequencies. In the Western Makran scenarios ($M_w$ 8.9 and 8.7), the high-frequency components (periods < 15 min) tend to arrive slightly earlier, followed by the high-energy, long-period components (periods > 30 min) which dominate the later phases. This is physically consistent with the physics of wave celerity in dispersive media. Crucially, the "red" zones of high energy are not short-lived flashes but appear as elongated bands stretching horizontally. This indicates that once the resonant frequencies (identified in Section 4.2) enter the domain, they excite the water column for a prolonged duration, likely due to the trapping of edge waves on the continental shelf. The magenta dashed line marks the initial arrival time, clearly showing that the bulk of the destructive energy (the "energy packet") lags behind the leading wave front by nearly an hour, a critical factor for safety protocols.

### 4.2.4 Hazard Duration in the Resonance Band

Standard spectral analyses, such as the Fourier transform presented in the previous section, assume stationarity and provide a time-averaged view of energy distribution. However, tsunamis are inherently non-stationary transient events where the energy content fluctuates significantly over time. To explicitly quantify the persistence of dangerous hydrodynamic conditions, we employed a Continuous Wavelet Transform (CWT) to compute the Scale-Averaged

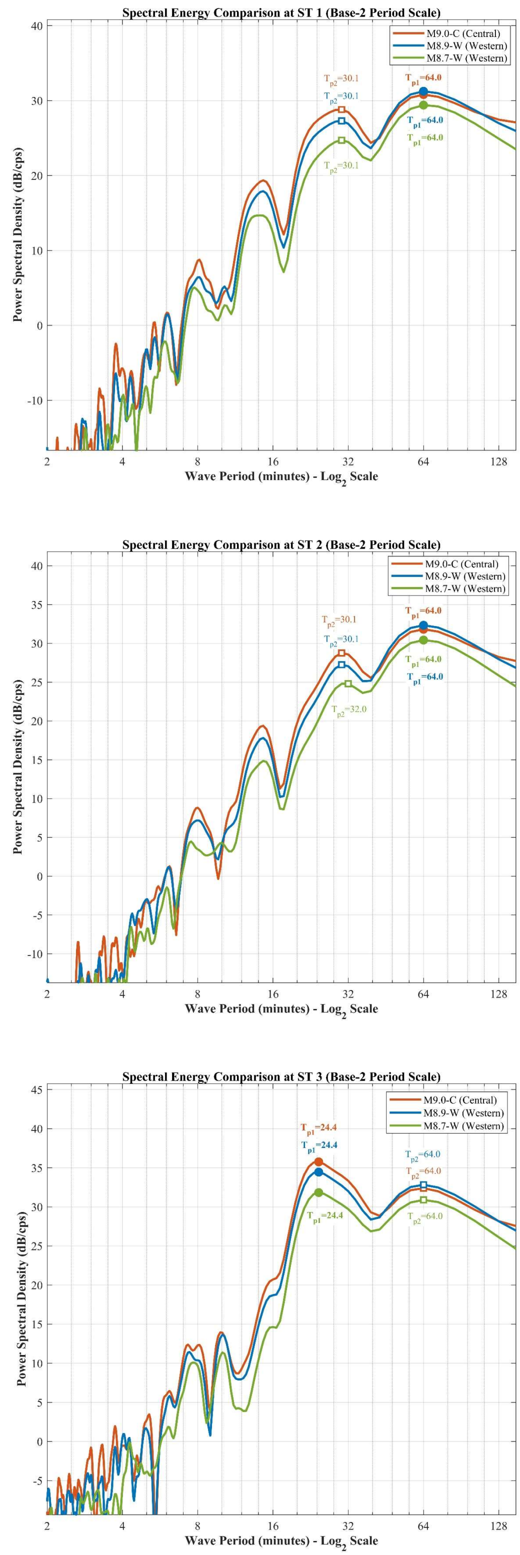


**Figure 7. Spectral energy density analysis for Offshore Station (ST 1 and ST 2) (depth~45-50 m) and nearshore station (ST 3) (depth ~10 m) , computed using Welch's periodogram method**

Wavelet Power (SAP). This analysis focuses specifically on the resonance-prone period band of 8 to 64 minutes, a critical range for medium-to-large harbor basins, as visualized in Figure 9.

A striking feature of the SAP profiles is the significant temporal lag between the initial wave arrival and the attainment of maximum spectral energy. While the leading wave reaches the Kooh Mobarak approximately 30–40 minutes post-rupture, the peak energy flux within the resonance band does not culminate until 2.2 to 2.3 hours after the earthquake. For the Central Makran scenario ($M_w$ 9.0), the peak power occurs at 2.2 hours, whereas for the Western scenarios ($M_w$ 8.9 and 8.7), it occurs slightly later at 2.3 hours. This delay indicates that the most destructive phase of the tsunami, in terms of its capacity to excite harbor oscillations and induce cyclical currents, is not driven by the initial wavefront. Instead, the maximum hydrodynamic stress arises from later wave packets, which are likely reinforced by multipath interference, shelf resonance, and the arrival of edge waves trapped along the continental shelf. This finding challenges the intuitive assumption that the first wave is invariably the most dangerous.

From an operational resilience perspective, the "Hazard Duration" is defined as the interval during which the wave energy exceeds a critical "Harbor Agitation Limit," conservatively set at 10% of the maximum peak power in this study. As depicted by the dashed threshold line in Figure 9, hazardous agitation levels persist for more than 4 hours post-event for all major scenarios. Even for the slightly smaller $M_w$ 8.7 Western scenario, the energy remains above the safety threshold well beyond the 4-hour mark. This prolonged duration of high-energy agitation has profound implications for post-disaster recovery. It suggests that maritime operations, such as the movement of support vessels or the re-berthing of tankers, cannot resume immediately after the passage of the initial wave train. Rather, a significant "exclusion window" of at least 5 to 6 hours must be enforced to ensure that the resonant energy within the basin has sufficiently decayed to levels safe for navigation and mooring operations.

## 4.3 Engineering Implications and Design Constraints

The integration of probabilistic hazard curves, spectral energy analysis, and momentum flux calculations provides a holistic set of constraints for the design and operation of the Kooh Mobarak future Terminal. Unlike conventional approaches that rely solely on

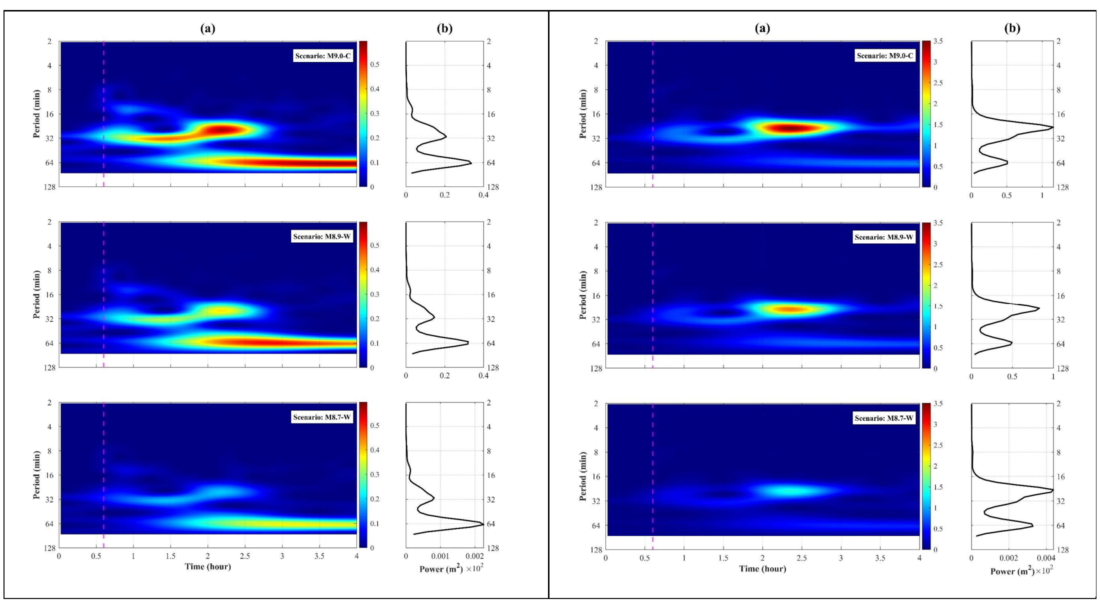


**Figure 8. Time-frequency analysis of the tsunami wave train at the offshore station (ST 1) (left panel) and nearshore station (ST 3) (right panel) using Continuous Wavelet Transform (CWT). The figure compares the spectral energy evolution for three governing rupture scenarios: Top row: Central Makran ($M_w$ 9.0), Middle row: Western Makran ($M_w$ 8.9), and Bottom row: Western Makran ($M_w$ 8.7). (a) Wavelet Power Spectrum (Scalogram). (b) Global Wavelet Spectrum. The vertical dashed magenta line indicates the initial tsunami arrival time (≈0.6 hours)**

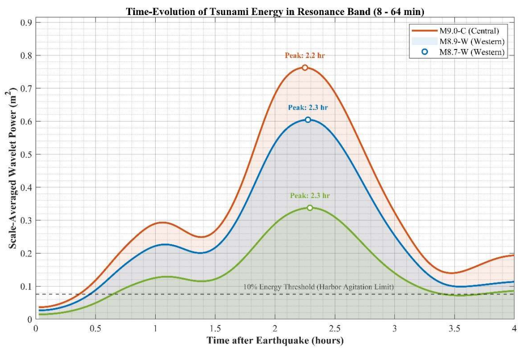


**Figure 9. Temporal evolution of tsunami energy within the critical resonance frequency band (periods of 8–64 minutes), calculated via Scale-Averaged Wavelet Power (SAP). The curves depict the energy flux for the three governing rupture scenarios: Central Makran ($M_w$ 9.0), Western Makran ($M_w$ 8.9), and Western Makran ($M_w$ 8.7).**

wave height, this study advocates for a multi-dimensional design philosophy that explicitly accounts for hydrodynamic force intensity, geometric resonance avoidance, and operational downtime windows.

### 4.3.1 Structural Vulnerability based on Momentum Flux

The stability of coastal structures, particularly breakwaters and quay walls, is more fundamentally governed by the Specific Momentum Flux ($M_F = hV^2$) than by flow depth alone. This parameter serves as a direct proxy for the hydrodynamic drag force and the potential for structural dislodgement. Figure 10 synthesizes the probabilistic hazard into a "Destructive Potential Curve," plotting specific momentum flux against the return period. The curve reveals a highly non-linear escalation of force, necessitating distinct design strategies for different performance levels.

#### 4.3.1.1 Serviceability Limit State (OBE - 475 Years):

At the Operating Basis Earthquake level (475-year return period), the specific momentum flux reaches approximately 3.0 $m^3/s^2$ . As illustrated in the figure, this value falls within Zone II (Moderate Structural Damage). From an engineering perspective, this implies that under OBE conditions, the breakwater armor units may experience partial displacement, and scour protection aprons will be subjected to significant shear stresses. Consequently, the design must ensure that such damage is "repairable" and does not compromise the core integrity of the port basin or lead to immediate operational shutdown. The armor layer weight calculations (e.g., using the Hudson or Van der Meer formulas) should utilize the velocity component derived from this flux value ($V \approx 2.1$m/s) rather than assuming a static standing wave.

#### 4.3.1.2 Ultimate Limit State (MCE - 975 Years):

For the Maximum Credible Earthquake (975-year return period), the hazard trajectory rises sharply into Zone III (Critical/Heavy Damage), with the momentum flux peaking at 12.3 $m^3/s^2$. This represents a four-fold increase in destructive force compared to the OBE level, despite the return period only doubling. This extreme flux indicates a potential for massive hydraulic loading capable of dislodging heavy concrete armor units (e.g., Antifer or Xbloc) and causing catastrophic scouring. Therefore, the design criterion for the MCE event must shift from "damage control" to "collapse prevention." To mitigate this risk, it is recommended to employ composite breakwater designs with reinforced toe protection and to consider the use of high-density concrete units for the most exposed sections of the breakwater head.

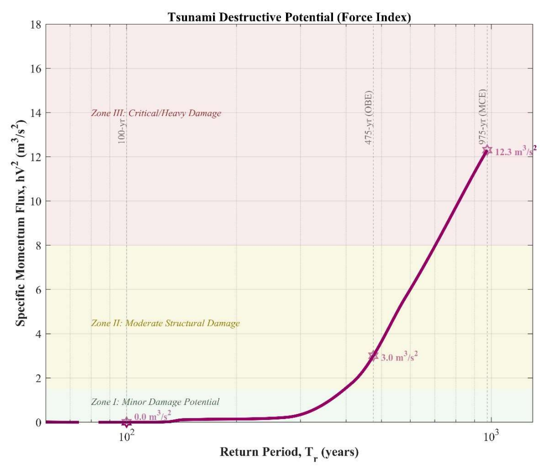


**Figure 10. Probabilistic assessment of tsunami destructive potential at the nearshore station, quantified by the Specific Momentum Flux ($M_F$=$hV^2$). The curve correlates the hydrodynamic force index with the return period, overlaid on empirical damage severity zones. Key design points are highlighted as Zone I (Green): Minor damage potential, relevant for frequent events (<100 years), Zone II (Yellow): Moderate structural damage, encompassing the Operating Basis Earthquake (OBE, 475-yr) with a flux of 3.0 $m^3/s^2$ that indicates that armor units may experience displacement but the structure retains core stability and Zone III (Red): Critical/Heavy damage, encompassing the Maximum Credible Earthquake (MCE, 975-yr) where the flux surges to 12.3 $m^3/s^2$**

### 4.3.2 Geometric Tuning for Resonance Avoidance

Beyond structural strength, the layout of the port basin itself serves as a passive defense mechanism. The spectral analysis (Section 4.2.2) identified two dominant tsunami energy bands centered around 24–30 and 64 minutes. To prevent destructive harbor resonance, the characteristic dimensions of the future basin must be "detuned" from these incoming frequencies. Utilizing the quarter-wavelength resonator principle derived in this study, port planners must avoid basin lengths that correspond to the critical resonant lengths ($L_{crit}$). Specifically, any proposed layout with a fundamental axis length approaching the values calculated in Section 6.2 should be modified, either by altering the dredging depth or changing the breakwater configuration, to shift the harbor's natural frequency away from the tsunami's high-energy spectral peaks. This proactive "geometric tuning" is a cost-effective non-structural mitigation strategy that significantly reduces the amplification of currents inside the basin.

### 4.3.3 Operational Resilience and Recovery

Finally, the time-frequency analysis (Section 4.2.3) dictates the protocols for emergency response and business continuity. The findings demonstrated that hazardous energy levels persist in the resonance band for over 4 hours, with the peak intensity occurring roughly 2.3 hours after the earthquake. This implies that the "All Clear" signal cannot be issued immediately after the first wave recedes. For the Jask terminal, an exclusion window of at least 6 hours post-event is recommended before allowing support vessels to re-enter the harbor or attempting to re-moor tankers. Furthermore, given the "leading depression" characteristic observed in the time-domain analysis, rapid-response protocols must mandate the immediate emergency unberthing of vessels to deeper waters (>50 m depth) to avoid hull grounding damages during the initial drawdown phase.

## 5. Conclusion

This study establishes a comprehensive, risk-informed framework for the protection of critical energy infrastructure in the northwestern Indian Ocean, specifically focusing on the Kooh Mobarak future Terminal near the strategic Strait of Hormuz. By integrating a high-resolution Probabilistic Tsunami Hazard Assessment (PTHA) with advanced spectral and time-frequency analyses, the research transcends traditional deterministic limitations to provide a multi-dimensional understanding of the tsunami threat. The investigation yields pivotal insights into the recurrence of extreme events, the hydrodynamic transformation of waves, and the frequency-dependent response of coastal basins.

The probabilistic analysis reveals that the tsunami hazard at Jask is governed by a complex interplay between source proximity and bathymetric amplification. The derived hazard curves exhibit a characteristic stepped morphology, reflecting the contribution of distinct tectonic segments ranging from frequent moderate earthquakes to rare mega-thrust events. A critical finding is the profound disparity between offshore and nearshore hazards; while offshore conditions are relatively benign, the nearshore zone experiences a drastic non-linear amplification of hydrodynamic forces. The developed Hydrodynamic Design Envelopes quantify this risk, establishing clear performance-based criteria. For the Serviceability Limit State (OBE, 475-year return period), the breakwater must withstand specific momentum fluxes corresponding to Zone II (Moderate Damage), requiring designs that allow for repairable displacement of armor units. Conversely, for the Ultimate Limit State (MCE, 975-year return period), the hazard escalates into Zone III (Critical Damage), where the momentum flux quadruples. This necessitates a design philosophy focused on collapse prevention through the use of high-density concrete armor units and reinforced toe protection to resist extreme scouring velocities exceeding 2.3 m/s.

Beyond amplitude and velocity, the spectral analysis using Welch's method uncovers the hidden frequency-domain risks. The identification of dominant energy peaks in specific period bands provides a crucial geometric constraint for future port development. To prevent destructive resonance, it is imperative that the characteristic dimensions of the port basin be "detuned" from these incoming spectral peaks. Furthermore, the time-frequency analysis via Continuous Wavelet Transform (CWT) challenges the conventional assumption that the initial wave arrival marks the moment of maximum danger. The results demonstrate a significant temporal lag, with the peak energy flux in the resonance band culminating approximately 2.3 hours after the earthquake and hazardous agitation persisting for over 4 hours. This finding dictates that emergency response protocols must enforce an extended exclusion window for maritime operations, prioritizing the evacuation of vessels to deep waters to avoid grounding during the leading depression phase and delaying re-entry until the resonant energy has sufficiently decayed.

Finally, the sensitivity analysis reinforces the necessity of a "Dual-Criterion" design approach for macrotidal regions. The study confirms that while the Mean High Water Springs (MHWS) condition represents the governing scenario for flood inundation and crest elevation due to higher total water levels, the Mean Sea Level (MSL) condition governs the design of scour protection systems due to higher particle velocities. Collectively, these findings advocate for a paradigm shift in the design codes for the Makran region, moving from single-scenario checks to a holistic resilience strategy that accounts for probabilistic exceedance, spectral resonance, and compound tidal interactions. This framework serves as a robust blueprint for securing strategic assets against the multi-faceted threat of tsunamis in the 21st century.

## References

Byrne, D. E., Sykes, L. R., & Davis, D. M. (1992). Great thrust earthquakes and aseismic slip along the plate boundary of the Makran subduction zone. *Journal of Geophysical Research: Solid Earth*, 97(B1), 449-478.

El-Hussain, I., Omira, R., Deif, A., Al-Habsi, Z., Al-Rawas, G., Mohamad, A., ... & Baptista, M. A. (2016). Probabilistic tsunami hazard assessment along Oman coast from submarine earthquakes in the Makran subduction zone. *Arabian Journal of Geosciences*, 9(1), 1-14.

Frohling, E., & Szeliga, W. (2016). GPS constraints on interplate locking within the Makran subduction zone. *Geophysical Journal International*, 205(1), 67-76.

Heidarzadeh, M., Pirooz, M. D., Zaker, N. H., Yalciner, A. C., Mokhtari, M., & Esmaeily, A. (2008). Historical tsunami in the Makran Subduction Zone off the southern coasts of Iran and Pakistan and results of numerical modeling. *Ocean Engineering*, 35(8-9), 774-786.

Heidarzadeh, M., Pirooz, M. D., Zaker, N. H., & Yalciner, A. C. (2009). Preliminary estimation of the tsunami hazards associated with the Makran Subduction Zone at the northwestern Indian Ocean. *Natural Hazards*, 48(2), 229-243.

Heidarzadeh, M., & Kijko, A. (2011). A probabilistic tsunami hazard assessment for the Makran subduction zone at the northwestern Indian Ocean. *Natural Hazards*, 56(3), 577-593.

Kazeminezhad, M. H., Akbarpour Jannat, M. R., & Rastgoftar, E. (2026). Deterministic Tsunami Hazard Assessment for a Nearshore–Onshore Domain close to the Strait of Hormuz: The Overlooked Threat of the Western Makran Segment and Tidal Sensitivity. *International Journal of Coastal, Offshore & Environmental Engineering*, 10(1).

Momeni, P., & Goda, K. (2024). Probabilistic tsunami hazard assessment for the Makran Subduction Zone using logic tree and stochastic rupture sources. *Coastal Engineering Journal*, 1-29.

Rabinovich, A. B. (2009). Seiches and harbor oscillations. In *Handbook of Coastal and Ocean Engineering* (pp. 193-236). World Scientific.

Rajendran, C. P., Ramanamurthy, M. V., Reddy, N. T., & Rajendran, K. (2008). Hazard implications of the late arrival of the 1945 Makran tsunami. *Current Science*, 95(12), 1739-1743.

Rashidi, A., Ortwin, R., & Sadeghi, M. (2020). Coastal vulnerability assessment of the Chabahar Bay due to tsunami hazard. *Natural Hazards*, 103, 2215–2234.

Salah, P., Sasaki, J., & Soltanpour, M. (2021). Comprehensive probabilistic tsunami hazard assessment in the Makran subduction zone. *Pure and Applied Geophysics*, 178, 5085-5107.

Smith, G. L., McNeill, L. C., Wang, K., He, J., & Henstock, T. J. (2013). Thermal structure and megathrust seismogenic potential of the Makran subduction zone. *Geophysical Research Letters*, 40(7), 1528-1533.

Titov, V. V., & Synolakis, C. E. (1998). Numerical modeling of tidal wave runup. *Journal of Waterway, Port, Coastal, and Ocean Engineering*, 124(4), 157-171.

Vernant, P., Nilforoushan, F., Hatzfeld, D., Abbassi, M. R., Vigny, C., Masson, F., ... & Bayer, R. (2004). Present-day crustal deformation and plate kinematics in the Middle East constrained by GPS measurements in Iran and northern Oman. *Geophysical Journal International*, 157(1), 381-398.

Wells, D. L., & Coppersmith, K. J. (1994). New empirical relationships among magnitude, rupture length, rupture width, rupture area, and surface displacement. *Bulletin of the Seismological Society of America*, 84(4), 974-1002.

Zafarani, H., Etemadsaeed, L., Rahimi, M., Kheirdast, N., Rashidi, A., Ansari, A., ... & Eskandari-Ghadi, M. (2022). Probabilistic tsunami hazard analysis for Western Makran coasts, South-East Iran. *Natural Hazards*, 115(2), 1275-1311.